LAWRENCE
LIVERMORE
NATIONAL
LABORATORY

LLNL-JRNL-855988

Development of an interatomic potential for the W-Ta system

B. Sharma, Y. S. Teh, B. Sadigh, S. Hamel, V. Bulatov, A. Samanta

October 16, 2023

Computational Materials Science

Disclaimer

Development of an interatomic potential for the W-Ta system

Bajrang Sharma[a,b], Ying Shi Teh[a], Babak Sadigh[a], Sebastian Hamel[a], Vasily Bulatov[c], Amit Samanta[a]

[a] *Physics Division, Lawrence Livermore National Laboratory, Livermore, California 94550, USA*
[b] *Department of Aerospace Engineering, Texas A&M University, College Station, Texas 77843, USA*
[c] *Materials Science Division, Lawrence Livermore National Laboratory, Livermore, California 94550, USA*

Abstract

A physics-inspired, data-driven interatomic potential framework for multi-element system is presented. This potential is based on the generalization of the embedded atom method potential and systematically incorporates two-, three- and many-body effects. Different atomic environments are described by atom-centered Gaussian basis sets which provides sufficient flexibility to capture diverse atomic environments and allows for easy optimization of the free parameters. An interatomic potential model for the tungsten-tantalum (W-Ta) system is developed using this framework by training on data from *ab initio* density functional theory (DFT) calculations. The potential is thoroughly tested at various compositions by comparing bulk and defect properties from experimental and DFT data. It is shown that the potential predicts the elastic constants, defect properties, such as vacancy and interstitial formation energies, core structures of dislocations, and melting points for both pure and tantalum and tungsten with an accuracy comparable to other single element machine learning based potentials. The potential model is used to investigate the formation energies of ordered alloys and vacancy formation energies for chemically random W-Ta alloys.

1. Introduction

Refractory metals, such as Ta, W, Nb, Mo and V, have attracted significant attention for high temperature structural applications due to their high melting points, mechanical strength and thermal conductivity. At ambient conditions these metals have body centered cubic (BCC) crystal structure and some of them (Nb, V and Ta) are ductile, while others, such as W and Mo, are brittle [1]. Therefore, binary, ternary as well as high entropy alloys consisting of refractory metals are promising candidates for high temperature structural applications, such as turbine blades of jet engines. In addition, W-Ta alloys have also been studied for plasma-facing armor or shielding components for fusion energy applications. According to the experimental phase diagram of the W-Ta system, Ta and W are miscible and do not form intermetallic phases at high temperature. However, Turchi et al. [2] using the tight-binding linear muffin-tin orbital formulation of the coherent potential approximation (TB-LMTO-CPA) predicted the formation of the B2 and DO_3 phases. Correspondingly, the predicted phase diagram (in Ref. [2]) shows a B2 phase which is stable up to about 1000 K. By using cluster expansion models based on a genetic algorithm search for interaction terms, Blum and Zunger [3, 4] predicted that $C11_b$ has lower energy than B2 and DO_3 ordered phases. However, by using a similar procedure, Muzyk et al. [5] found the ground state structure to be W_5Ta_3. Given this discrepancy in the ground state structures predicted using different methods, i.e., CPA and cluster expansion models, it is instructive to find other way (such as developing interatomic potentials) to resolve this conundrum.

Embedded atom method (EAM)[17, 18] potentials have been successfully used to model phase transitions and dislocation properties in metals that have close packed crystal structure, like Cu and Al. But for BCC metals that have a lower packing density than closed packed structures, EAM potentials are typically unable to accurately capture one or more of these properties (see Tables 1 and 2): (a) phonon dispersion curves, (b) ground-state core structure of a screw dislocation and (c) formation energies of point defects, like mono-vacancy and self-interstitials in $\langle 111 \rangle$, $\langle 110 \rangle$, $\langle 100 \rangle$ dumbbell configurations. Significant advancement in recent years, particularly due to the development of angular-dependent potential (ADP) [19], spectral neighbor analysis potential (SNAP)[14, 13], Gaussian approximation potential (GAP)[20] and other machine learning formalisms [21, 22], have led to the development of more accurate potentials for BCC metals in which these properties are correctly modeled [23]. These newer potentials include explicit three-body (and four-body in some cases) interactions and incorporate angular effects, both of which are absent in the EAM formalism. However, the computational cost of these potentials is much higher than EAM or modified EAM (MEAM) potentials [24]. In addition, the number of structures needed to train such potentials is also significantly higher than those required to train EAM potentials. Therefore, it is desirable to develop potentials that have high accuracy (similar to GAP) [24] in predicting physical properties but need fewer structures to train and at the same time is not as expensive as GAP.

While potentials for BCC refractory metals have improved in the last few years, unfortunately, potentials for alloys are still not as accurate as those available for constituent metals. For instance, three and four body interactions are included in newer potentials for Ta and W (such as SNAP, GAP and ADP). How-

Email address: samanta1@llnl.gov (Amit Samanta)

	GEAM	DFT	EXP [6]	EAM [7, 8]	MEAM [9]	FS [10, 11]	GAP [12]	SNAP [13, 14]	PINN [15]	ADP [16]
Ta										
a (Å)	3.321	3.319	3.303	3.303		3.304	3.321	3.316	3.3203	3.304
E_{bcc} (eV/atom)	−11.813	−11.813					−11.813			
C_{11} (GPa)	264	270	260	248.6	266	267	267	270	269	268.9
C_{12} (GPa)	162	156	154	144.6	158	158	161	151	163	157.6
C_{44} (GPa)	71.4	74	83	86.5	87	87.3	77	73.4	72	90.4
W										
a (Å)	3.186	3.185	3.165	3.185		3.165	3.185	3.180		
E_{bcc} (eV/atom)	−12.955	−12.957					−12.956			
C_{11} (GPa)	526	515	522	523	532.6	522	524	518		
C_{12} (GPa)	202	194	204	203	205	204	200	195		
C_{44} (GPa)	154	152	161	160	163	161	148	144		

Table 1: Ground state energies (E_{bcc}), lattice parameter (a) and elastic constants (C_{ij}) of the BCC phase for pure W and Ta. For comparison, physical properties determined from DFT calculations (performed in this work), experiments and other single element potential models are also listed.

ever, the most recent potential for the W-Ta alloy is based on the Finnis-Sinclair (FS) formalism and does not include angular effects in modeling the interaction between W and Ta atoms. One potential consequence of the absence of three-body interaction term is that the FS potential for W-Ta is unable to correctly predict the ground-state structure of ordered alloys. Therefore, exploring the effect of higher order correlations in potentials for alloys becomes important because Dudarev and co-workers [25, 26] have shown that clusters containing four and five atoms are needed to generate predictive cluster expansion models for Ta-W and V-W. In this work, we generalize the EAM framework to include three-body and higher order interactions and use basis functions to model the two-body, three-body and higher order interaction. This potential framework, which we call GEAM, i.e. generalized EAM, allows us to include physics via the different interaction terms and provides sufficient flexibility to model different atomic environments. The GEAM framework is then used to develop a potential for the W-Ta binary system which is systematically tested and validated for a wide range of conditions.

2. Numerical Methodology

In this section, we present a interatomic potential framework for multi-element system. The training dataset, optimization procedure and MD simulation details are also discussed.

2.1. Interatomic Potential Model

The potential framework used in the current work is based on a generalization of the embedded atom method. The total energy of a system in the EAM framework is modeled by the sum of a pair and many body interactions, where the later embeds the local density around an atom by using a non-linear function. In the past few years, researchers have proposed many different schemes to generalize EAM potentials to overcome the limitations mentioned previously, but many such models rely on fixed functional forms which limits the flexibility of the proposed potentials. To design flexible EAM potentials, spline-based model fitting procedures have also been used but extensive tests are often necessary to obtain smooth potentials [19].

Building on the previous work of Ref. [28] we present a GEAM based potential framework for binary systems in which the total energy, E, is given by the following relation

$$E = E_{\text{em}} + E_{32} + E_{\text{nl}}. \tag{1}$$

The first term E_{em} is inspired by the embedding energy in classical EAM model and incorporates sufficient flexibility (beyond what is possible in traditional EAM potentials) into the GEAM model. The atomic density used to model this embedding energy is approximated by a few atom-centered, even-tempered Gaussian basis functions. The even-tempered Gaussian basis sets have been successfully used for electronic structure calculations because it has been shown that they span the Hilbert space evenly [29]. We conjecture that using these basis functions will provide the flexibility to learn a variety of functional forms. The resulting models can therefore mimic a diverse set of atomic environments. Motivated by the machine learning potential formulation presented in Ref. [22, 30] the embedding energy is expressed as a Taylor series expansion and takes the following functional form

$$\begin{aligned} E_{\text{em}} &= \sum_{i=1}^{N_{\text{tot}}} \left[C_0^{e_i} + \sum_{m=1}^{M_{\text{e}}} \sum_{n=1}^{N_{\text{e}}} C_{mn}^{e_i} (\rho_i(n))^m + \sum_{n=1}^{N_e} \tilde{C}_n \left|\nabla \rho_i(n)\right|^2 \right] \\ \rho_i(n) &= \sum_j e^{-\beta_n^{e_j} r_{ij}^2} f_s(r_{ij}, r_{\text{c}}); \; \forall\, n \in [1, N_e]. \end{aligned} \tag{2}$$

Here, N_{tot} is the total number of atoms, M_{e} is the order of the embedding polynomial, N_{e} is the number of Gaussian basis functions used to represent the atomic density ρ_i, r_{ij} is the distance between atoms i and j, r_{c} is a cut-off radius and $\beta_n^{e_j}$ are the widths of the Gaussian basis functions. The superscript e_i, e_j denotes the elemental types of atoms i and j: For example, the Gaussian widths $\beta_n^{e_j}$ depend on the element type to incorporate the effect of chemistry in the atomic density. The even-tempered approach, which is popular in basis-sets used for *ab initio* calculations [31, 32, 33], is employed to minimize

	GEAM	DFT [26, 25]	EXP [27]	EAM [7, 8]	MEAM [9]	FS [10, 11]	GAP [12]	SNAP [13, 14]	PINN [15]	ADP [16]
Ta										
E_f^{vac} (eV)	2.96	2.95	3.09	2.76	2.95	3.07	3.09	2.74	2.772	3.06
$E_f^I\langle 111\rangle$ (eV)	5.245	4.77		6.53	4.88	5.75	4.84	5.74	4.687	5.62
$E_f^I\langle 110\rangle$ (eV)	5.324	5.48		6.10		6.15	5.47	5.43	5.414	5.65
$E_f^I\langle 100\rangle$ (eV)	5.893	5.89		8.04		6.82	5.99	6.89	5.820	5.86
E_f^I OCTA (eV)	6.04	5.95					6.06	7.10	5.986	
W										
E_f^{vac} (eV)	3.35	3.36	3.32	3.59	3.95	3.54	3.36	3.21		
$E_f^I\langle 111\rangle$ (eV)	10.23	10.29		10.53	8.98	9.46	10.35	9.7		
$E_f^I\langle 110\rangle$ (eV)	10.99	10.58		10.83		9.80	10.58	9.8		
$E_f^I\langle 100\rangle$ (eV)	11.14	12.20		12.89		11.01	12.23			
E_f^I OCTA (eV)	11.67	12.27		13.16		10.71	12.33	11.5		

Table 2: Formation energies of vacancies and self-interstitial atoms in different configurations in W and Ta. For comparison, formation energies obtained from DFT calculations [26, 25], experiments and other single element potential models are also listed.

the total number of free parameters. Thus, the widths are expressed as $\beta_n^{e_j} = \alpha_0^{e_j}(\beta_0^{e_j})^{n-1}$, which reduces the number of free parameters to two for each elemental type.

A smooth decaying function, f_s, is included in the density expansion to ensure a smooth transition to zero at the cut-off point, r_c,

$$f_s(r, r_c) = \begin{cases} (1 - r/r_c)^4 & \text{for } r < r_c \\ 0 & \text{for } r \geq r_c \end{cases} \quad (3)$$

The smoothing function f_s as well as its first, second and third derivatives decay to zero at $r_{ij} = r_c$.

In E_{em}, the pair interaction term is modeled by $m = 1$ and $m \geq 2$ corresponds to higher order interactions. A term based on the gradient of atomic density ($\nabla\rho_i$) is also included in the embedding function to better capture large electron-density gradients around defects [34].

The second term in Eq. (1) is the three-body E_{32} interaction term and contains explicit angular dependence. Following previous interatomic potential models [35, 36], we also model three-body interactions by a product of radial and angular terms.

$$E_{32} = \sum_{\substack{\langle i,j,k\rangle \\ k\neq i \\ k>j}} \left[\hat{E}_{32}^{e_ie_je_k}(r_{ij}, r_{ik}) f_s(r_{ij}, r_c) f_s(r_{ik}, r_c)\right] P(cos\theta_{jik}), \quad (4)$$

where, r_{ij} and r_{ik} are the distances between atom i and its neighbors j and k, θ_{jik} is the angle subtended at atom i by the triplet $\langle i, j, k\rangle$. To ensure that the chemical environment is adequately modeled, the radial component of three-body potential ($\hat{E}_{32}$) is expanded using Gaussian basis functions for each unique chemical triplet.

$$\hat{E}_{32}^{e_ie_je_k} = \sum_{m=1}^{N_{32}} \sum_{n\geq m}^{N_{32}} \hat{C}_{mn}^{e_ie_je_k} \left[e^{-\hat{\beta}_m r_{ij}^2 - \hat{\beta}_n r_{ik}^2} + e^{-\hat{\beta}_n r_{ij}^2 - \hat{\beta}_m r_{ik}^2}\right] \quad (5)$$

The widths $\hat{\beta}_m$ and $\hat{\beta}_n$ are also contracted by the geometric sequence $\hat{\beta}_n = \hat{\alpha}_0\hat{\beta}_0^{n-1}$ and a polynomial expansion of the angle θ_{jik} is used to model the angular part of the three-body term, i.e.,

$$P(cos\theta_{jik}) = 1 + \sum_{p=1}^{N_{p32}} c_p (cos\theta_{jik})^p, \quad (6)$$

where N_{p32} is the order of the polynomial used to model the angular contributions.

The discussion in the preceding paragraphs focuses on developing a flexible and easy-to-fit procedure to capture two- and three-body interactions. These two contributions are typically included in most empirical and machine learning potentials and the underlying assumption of such a formulation is that the relevance of contributions from higher order interactions decreases as we go to four-body or higher order terms. Therefore, even though in principle this procedure can also be used to construct higher order interaction terms, such terms are usually not included because the computational cost increases exponentially, i.e. scales as $O\left(N_{nn}^p\right)$, where N_{nn} is the number of neighbors and p is 1 for pair, 2 for three-body and 3 for four-body interactions. Therefore, one can ask if it is possible to construct nonlinear "composite" features from these two and three-body terms, which can incorporate additional physics, such as, those present in higher order many-body interactions, at a significantly reduced cost than that is required in case of a four-body interaction term. To this end, we use symbolic regression to discover mathematically interpretable relations in an intelligent and non-intuitive way directly from the training data[37, 38]. We use the GPTIPS toolbox to carry out the symbolic regression analysis [39] .

A non-local term, (E_{nl}), in Eq. 2 is inspired by such a symbolic regression based analysis and has the following functional form:

$$E_{nl} = \sum_{i=1}^{N_{tot}} \sum_{n=1}^{N_{nl}} \left[\overline{C}_n^1 \sqrt{\Psi_i^2(n)} + \overline{C}_n^2 \sqrt{\Psi_i^4(n)} + \overline{C}_n^3 \sqrt[4]{\Psi_i^4(n)}\right] \quad (7)$$

Here, N_{nl} is the number of Gaussian basis functions, $\Psi_i^m(n)$ is

the effective (non-local) density of atom i and includes contributions from neighbors of i via the following relationship:

$$\Psi_i^m(n) = (\psi_i(n))^m + \sum_j \left(\psi_j(n)\right)^m f_s(r_{ij}, r_c) \tag{8}$$

where, $m = 2$ or 4. The local density $\psi_i(n)$ is also expanded using Gaussian basis functions, i.e.,

$$\psi_i(n) = \sum_j e^{-\overline{\beta}_n^{e_j} r_{ij}^2} f_s(r_{ij}, r_c); \quad \overline{\beta}_n^{e_j} = \overline{\alpha}_0^{e_j} (\overline{\beta}_0^{e_j})^{n-1}. \tag{9}$$

The inclusion of the non-local term in our model has two key advantages: (i) higher-order many body correlations are incorporated at modest computational effort and (ii) thorough testing of the model has revealed that the non-local term is important for high temperature stability of the model, especially in modelling the melting temperatures.

2.2. Training Dataset

An interatomic potential for the W-Ta alloy is trained using total energies and forces obtained from DFT calculations. The training set contains 336 different structures and includes: (i) bulk structures with varying degrees of compression and shear, (ii) defect structures including vacancies, interstitials and grain boundaries, (iii) structures from cluster expansion models and (iv) a few liquid structures. As shown in Fig. 1, the training set includes many structures for pure Ta and W (to ensure that properties of pure elements are modeled with very high accuracy) as well as structures at various intermediate global chemical compositions of the W-Ta alloy to ensure sufficient representation of different chemical environments. A detailed description of the structures included in the training set is given in Table 4 of Appendix A. We purposefully do not include any structures with global tungsten composition $x_W \in [0.6, 0.8]$ to gauge the potential's ability to interpolate in the chemical space. As we demonstrate in the following sections, this small, yet diverse, set of structures is sufficient to capture structural as well as chemical changes in the system.

All DFT calculations in the present work are performed using the Vienna Ab initio Simulation Package (VASP) [40, 41] with the projector augmented wave (PAW) pseudopotentials containing 14 and 11 valence electrons for W and Ta, respectively, the PBE functional and a smearing width of 0.10 eV. We use a cut-off energy of 450 eV for the plane-wave basis set and a 6×6×6 Monkhorst-Pack mesh for a system size of about 16.5×16.5×16.5 Å^3 (containing 250 atoms) or the equivalence of such a mesh depending on the system size. The convergence criterion for self-consistent field calculations is set to 10^{-7} eV.

2.3. Training Procedure

The coefficients, $C = \{C_0, C_{mn}, \tilde{C}_n, \overline{C}_n^k, \hat{C}_{mn}^{e_i e_j e_k}, \}$ and the widths of the Gaussian basis functions, $\Omega = \{\alpha_0^{e_j}, \beta_0^{e_j}, \hat{\alpha}_0, \hat{\beta}_0, \overline{\alpha}_0^{e_j}, \overline{\beta}_0^{e_j}\}$, are optimized by using an iterative procedure that involves solving a linear system of equations to solve for C for fixed values of widths (in the inner loop) and optimizing the widths using the Nelder-Mead simplex method (implemented in Matlab) in the outer loop. This iterative procedure, minimizes a loss function, $\mathcal{J}_1$, constructed from the deviation of model predictions from DFT energies and forces, i.e.,

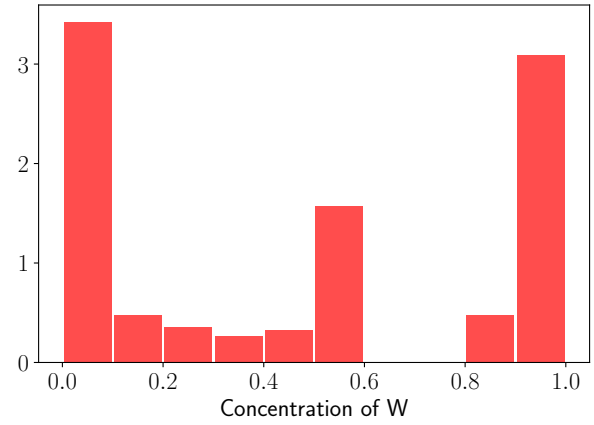

Figure 1: Distribution of global tungsten composition in the training dataset. Note that no structures with $x_W \in [0.6, 0.8]$ are included to gauge the ability of the potential to interpolate in the chemical space.

$$\min_{C,\Omega} \left\{ \mathcal{J}_1(C, \Omega; c_p) = \left\| A(\Omega; c_p) C - b \right\|_2^2 \right\}, \tag{10}$$

where A contains features corresponding to EAM, three-body and nonlinear terms in our model, b is a vector containing forces and energies computed from DFT simulations and c_p are the coefficients of the polynomial expansion for the angular term defined in Eq. (6). The loss function $\mathcal{J}_1$ is optimized for a fixed set of angle coefficients, c_p, all of which are initially set to zero at the beginning of the optimization. The Gaussian widths are initialized by setting $\alpha_0, \hat{\alpha}_0, \overline{\alpha}_0 = 0.01$ and $\beta_0, \hat{\beta}_0, \overline{\beta}_0 = 1.6$ [28].

After obtaining an optimal set of Gaussian widths and coefficients for the embedding energy, nonlinear term and the three-body interactions, the coefficients for the angle terms are obtained by solving another set of linear equations. Since the total energies and forces also vary linearly with the angle coefficients, the optimization problem can be expressed in terms of the coefficients $\overline{C} = \{C_0, C_{mn}, \tilde{C}_n, \overline{C}_n^k, c_p\}$ and the widths Ω

$$\min_{\overline{C},\Omega} \left\{ \mathcal{J}_2(\overline{C}, \Omega; \hat{C}_{mn}^{e_i e_j e_k}) = \left\| A(\Omega; \hat{C}_{mn}^{e_i e_j e_k}) \overline{C} - b \right\|_2^2 \right\}. \tag{11}$$

Note that the coefficients associated with three-body interactions, i.e., $\hat{C}_{mn}^{e_i e_j e_k}$, are fixed during this optimization.

For a fixed set of Gaussian widths, the functions $\mathcal{J}_1$ and $\mathcal{J}_2$ are minimized iteratively to obtain the optimal coefficients for the embedding energy, nonlinear term and the three-body interactions. One of the major advantages of the current framework is that the objective functions $\mathcal{J}_1$ and $\mathcal{J}_2$ are convex in the coefficient space C and $\overline{C}$, respectively. Consequently, the parameters C and $\overline{C}$ can be accurately optimized using linear regression at modest computational expense.

The model hyperparameters $\mathcal{H} = \{M_e, N_e, N_{32}, N_{p32}, N_{nl}\}$ are optimized by using an extensive grid search and the opti-

M_e	N_e	N_{32}	N_{p32}	N_{nl}
4	8	4	12	6

Table 3: Hyperparameters of the GEAM interatomic potential.

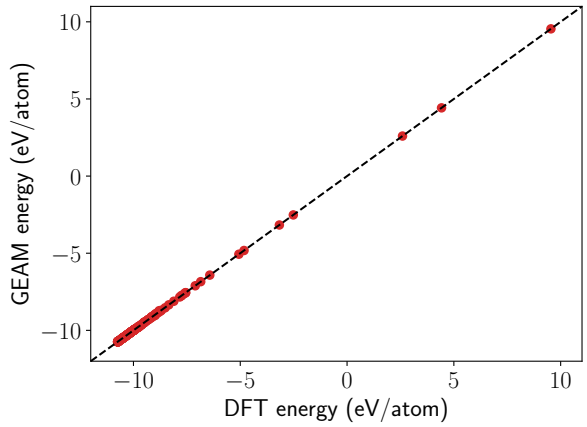

Figure 2: Energies of structures in the training set computed with the GEAM potential against the DFT energies. The dashed line represents the ideal fit.

mized hyperparameters are listed in Table 3. For the set of optimized hyperparameters listed in Table 3, the model has a total of 182 free parameters. The optimized parameters, including the widths Ω, the coefficients C and c_p are listed in Tables 5-9 of Appendix B.

The cut-off radius is selected as $r_c = 6$ Å, such that interactions between an atom and neighbors in the first five coordination shells of the ideal BCC lattice are included in the potential. In addition, increasing the cut-off distance to include the sixth coordination shell does not result in a better potential.

To analyze the performance of the model on the training set, we compare the model energy predictions with the DFT energies in Fig. 2. The overall root mean square error (RMSE) calculated from the loss function $\mathcal{J}_1$ (in Eq. 10) on the training set is 0.1231. Note that this RMSE score includes both deviations in total energies and forces. The RMSE for the force predictions is 0.103 eV/Å. The mean absolute error (MAE) for the predicted total energies is 4.13 meV/atom and is comparable to the machine learning based potential for a similar binary system reported in Ref. [42]. It is worth noting that machine learning based potentials are typically trained on a much larger training data set. For instance, the Gaussian approximation potential (GAP) for W-Mo alloy [42] was trained using approximately 9000 structures, which is an order of magnitude more than the 336 training structures used in this work. In general, training data generation from DFT calculations is the slowest part of the potential development process. Therefore a model based on the GEAM framework can be potentially advantageous as it can substantially improve the turnaround time for potential development.

2.4. MD Simulations

The GEAM potential for W-Ta alloy is implemented in the massively parallel molecular dynamics simulator LAMMPS [43]. All MD simulations in this work are performed in LAMMPS using a time step of 2 fs.

3. Validation of the potential model

We validate and test the GEAM model for W-Ta alloys in two stages. First, physical properties, such as elastic constants, equation of state, phonon dispersion curves, and defect properties, such as vacancy and interstitial formation energies, in pure tantalum and tungsten are compared against DFT and experimental data. Next, to assess the chemical accuracy, total energies and a variety of physical properties calculated from the GEAM potential and DFT for structures containing random or ordered distribution of the elements are compared at various compositions.

3.1. Bulk Properties of W and Ta

The equation of state for the BCC phase of both W and Ta are presented in Fig. 3. The cold curves predicted from the GEAM potential are in excellent agreement with DFT data meaning that the potential is able to accurately capture the ground state energies of both W and Ta.

The ground state energies, E_{bcc}, equilibrium lattice parameters and elastic constants, including C_{11}, C_{12} and C_{44} (calculated using the procedure described in Ref. [44]), for both W and Ta in BCC phase are listed in Table 1. To assess the quality of predictions, data from current DFT calculations, experimental results [6] and predictions from other single element interatomic potentials available in the literature are also listed in Table 1. Specifically, the model predictions are compared against potentials for W and Ta developed using the following methods: (i) the EAM [7, 8], (ii) modified-EAM (MEAM) [9], (iii) Finnis-Sinclair [10, 11], (iv) Gaussian approximation potential (GAP) [12], (v) spectral neighbor analysis method (SNAP) [13, 14], (vi) physically informed neural network (PINN) [15] and (vii) angular dependent potential (ADP) [16]. It is clear from Table 1 that the ground state energies and the equilibrium lattice parameters are predicted with high accuracy by the GEAM potential. In addition, the elastic constants C_{11}, C_{12} and C_{44} for both pure W and Ta obtained from the GEAM potential are within 4% of the DFT values. Overall, the accuracy of the physical properties is much better than existing semi-empirical potentials and on par with machine learning potentials based on GAP and SNAP (which typically require a much larger training set) frameworks.

To further assess the performance of the potential, we compare the phonon dispersion curves obtained from GEAM potential and DFT in Fig. 4 calculated by using the open-source Phonopy package [45]. The harmonic properties of pure W and Ta are adequately captured by the model along several high symmetry directions for both transverse and longitudinal acoustical branches thereby demonstrating that model predictions are in good agreement with the current DFT calculations. Note that

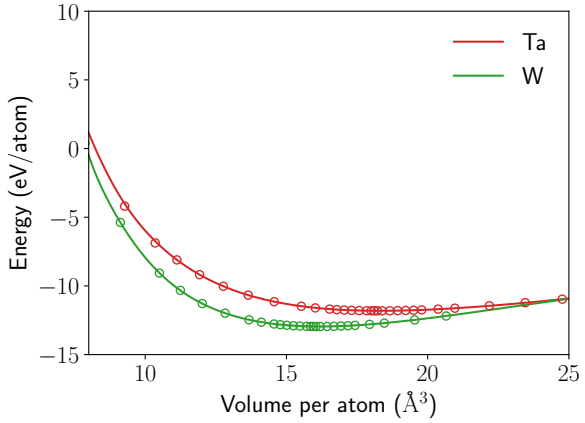

(a) Energy-Volume curve

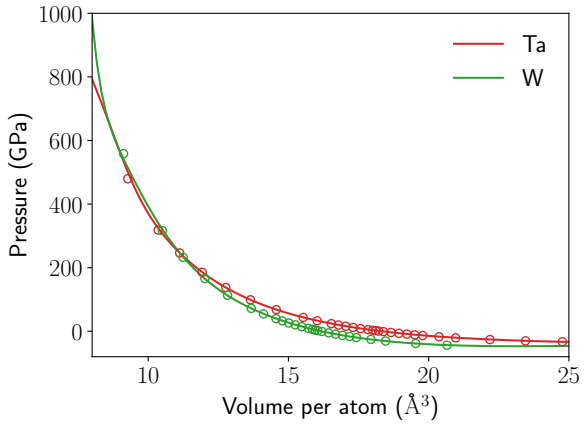

(b) Pressure-volume curve

Figure 3: Equation of state for bcc phase of pure tungsten and tantalum: (a) energy-volume and (b) pressure-volume. The solid lines correspond to predictions from the GEAM potential and symbols are results obtained from DFT calculations.

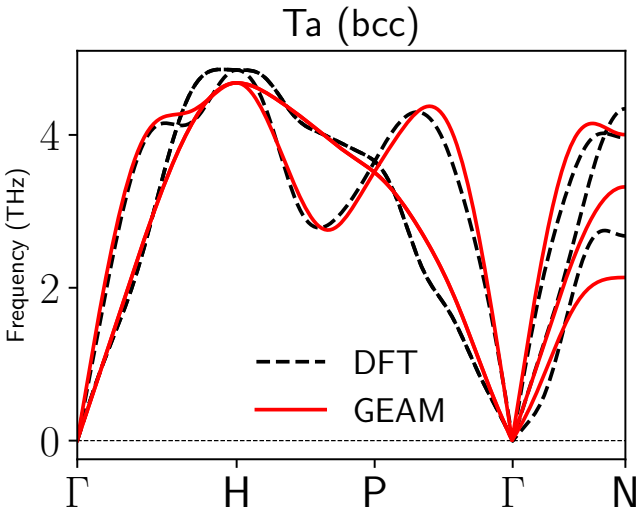

(a)

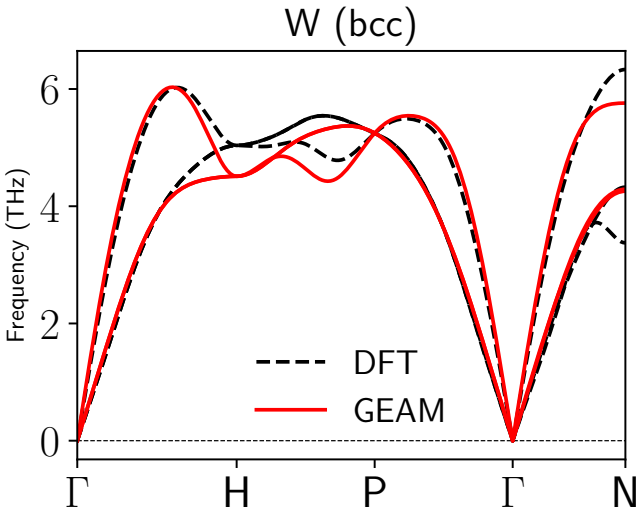

(b)

Figure 4: Phonon dispersion curves for BCC phase of pure (a) tantalum and (b) tungsten. Red solid lines correspond to phonon curves from the GEAM potential and black dashed lines represent our DFT calculations.

no information about phonon dispersion curves are included in the training set, which is in contrast to other machine learning potentials, such as GAP [12], wherein phonon data is used for training purposes. The overall agreement of the current phonon curves is much better than the single-element bond order potentials (BOPs) of Ref. [46] and the accuracy is comparable to the GAP potentials [12] for W and Ta.

3.2. *Point defects in W and Ta*

To ensure that defect properties are captured accurately by the GEAM potential, we include data for vacancies and some self-interstitial atom (SIA) configurations, including interstitials in ⟨110⟩ dumbbell, ⟨100⟩ dumbbell, ⟨111⟩ crowdion and the octahedral geometries, in the training set. The formation energies of vacancies and interstitials for both W and Ta predicted using the GEAM potential are listed in Table 2. To evaluate these defect formation energies, we remove or insert an atom into a supercell containing 250 Ta or W atoms which is obtained by replicating the BCC conventional unit cell $5\times5\times5$ along the three different axes. As shown in Table 2, the vacancy and interstitial formation energies in pure Ta and W are predicted within a few percent (less than 10%) of the DFT values suggesting that the environments around these defects are accurately modeled.

In agreement with previous DFT results [25, 26], the current model predicts that the axially symmetric ⟨111⟩ SIA as the most stable configuration for both W and Ta. Moreover, the ordering for the formation energies of SIA configurations are also in agreement with DFT results [25, 26]. Note that the ordering of interstitial formation energies (for different SIA configurations) do not always agree with DFT results for the pure Ta or W potentials based on the EAM [7], Finnis-Sinclair [11] and SNAP [13] frameworks. In our potential, the largest discrepancy is observed for the ⟨111⟩ crowdion of Ta, where the model over predicts the DFT value by 0.8 eV which translates to an error of about 3.2 meV/atom in a supercell with 251 atoms and as such is below the MAE for energy predictions in the training set (see Section 2.3).

3.3. *Bulk properties of W-Ta alloy: Effect of chemistry on lattice parameter*

To ensure that chemical effects are accurately modeled, we test the physical properties, such as elastic constants, lattice parameters and enthalpies of mixing for the BCC phase of the W-Ta alloy at different chemical compositions. To this end, the equilibrium lattice parameters $a(x_W)$ of chemically random W-Ta alloys are presented in Fig. 5(a) and compared with results reported in the literature. Note that except for the lattice parameters for pure W and Ta, no information about the equilibrium structures is present in the training set.

At each composition, a lattice parameter is obtained (by using the GEAM potential) by relaxing a random distribution of 2000 atoms on a 10×10×10 BCC supercell. The equilibrium lattice parameter for a given composition is then obtained by averaging the lattice parameter over 5 different realizations of the random distribution. The final lattice parameters predicted

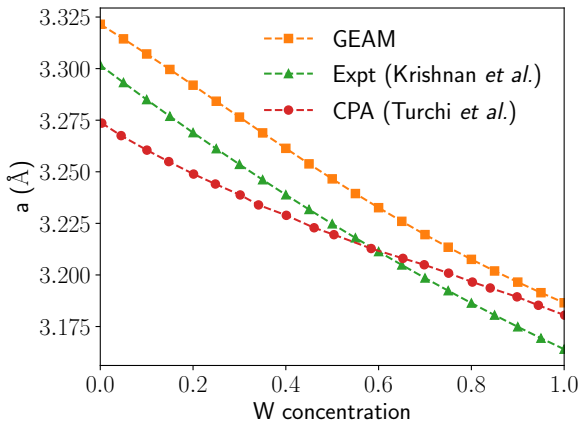

(a)

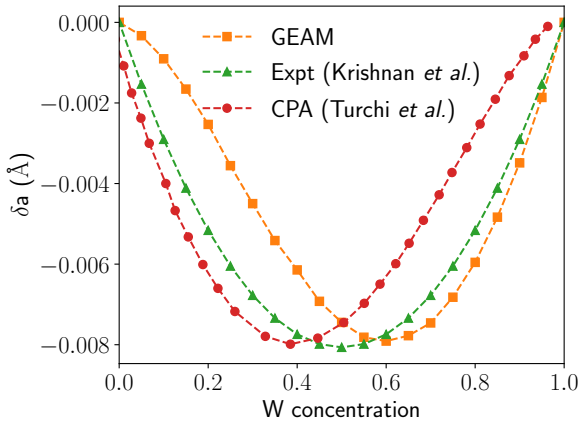

(b)

Figure 5: Variation of the (a) lattice constant and (b) departure of lattice constant from Vegard's law for chemically random W-Ta alloys. Filled squares correspond to results from our GEAM potential model, experimental results from Ref. [47] and CPA calculations of Ref. [2] are marked with triangles and circles respectively.

from this procedure agrees well with experimental results detailed in [47] and lattice parameters obtained from coherent potential approximation (CPA) [2]. In fact, the error in model predictions compared to experimental results is less than 1% and this small discrepancy can be attributed to the difference in experimental and DFT lattice parameters of pure metals.

The departure of the lattice parameter from Vegard's law, δa, is defined as

$$\delta a(x_W) = a(x_W) - x_W a_W - (1 - x_W) a_{Ta}, \qquad (12)$$

and is displayed in Fig. 5(b). Here x_W is the concentration of tungsten, a_W and a_{Ta} are the equilibrium lattice parameters for pure W and Ta, respectively. Although small discrepancies between experimental and GEAM values are observed near the dilute limit of tungsten, the overall trends are adequately captured across the entire chemical space. This confirms that the potential captures higher order chemical effects and is able to properly model a rich variety of chemical environments even

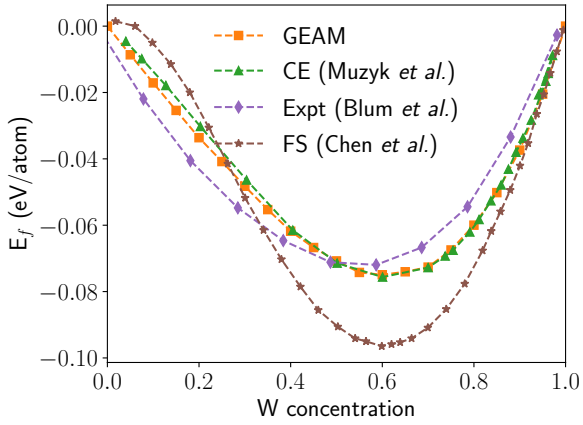

Figure 6: The enthalpies of mixing for chemically random W-Ta alloys. Orange squares correspond to results obtained from our GEAM potential, enthalpies from cluster expansion model of Ref. [5] are marked using green triangles, purple diamonds represent experimental results from Ref. [4] and results from the Finnis-Sinclair type potential of Ref. [11] are marked using brown stars.

though the training structures (see Fig. 1) do not span the whole composition space.

3.4. Bulk properties of W-Ta alloy: Enthalpy of mixing

The enthalpy of mixing E_f for the W-Ta alloy is defined as follows:

$$E_f(x_W) = \frac{E(x_W)}{N_{tot}} - x_W e_W - (1 - x_W) e_{Ta}. \quad (13)$$

Here, $E(x_W)$ is the total energy of the W-Ta alloy, N_{tot} is the number of atoms in the alloy, e_W and e_{Ta} are the ground-state energies (i.e., chemical potentials) for the BCC phase of pure W and Ta, respectively. The mixing enthalpies for chemically random W-Ta alloys are presented in Fig. 6. For comparison, the mixing enthalpies of the special quasirandom structures (SQS) obtained using cluster expansion (CE) [5], experimental results from Ref. [4] and predictions from a Finnis-Sinclair type interatomic potential for the W-Ta alloy [11] are also included in Fig. 6. In accordance with previous CE calculations, the current model predicts that the most stable alloy configuration is tungsten rich at $x_W \approx 0.6$. The formation enthalpies for the most stable composition and for structures at the dilute limits of both W and Ta are well replicated indicating that the effect of chemistry is well captured in the potential. Based on the enthalpy computations from the GEAM potential, a polynomial fit for the ground-state of the random W-Ta alloy is detailed in Eq. (14)

$$E_f(x_W) = 0.28x_W^6 - 0.871x_W^5 + 1.129x_W^4 - 0.487x_W^3 + 0.131x_W^2 - 0.181x_W. \quad (14)$$

3.5. Bulk properties of W-Ta alloy: Effect of chemistry on elastic constants

The mechanical properties of the chemically random W-Ta alloy are assessed next. Similar to the calculation of lattice parameters, the elastic constants are calculated using a random

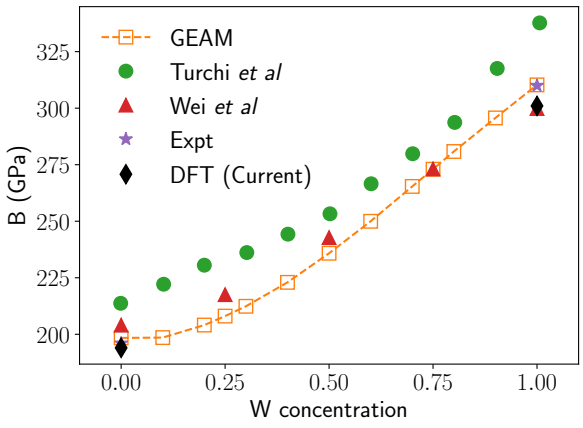

(a) B

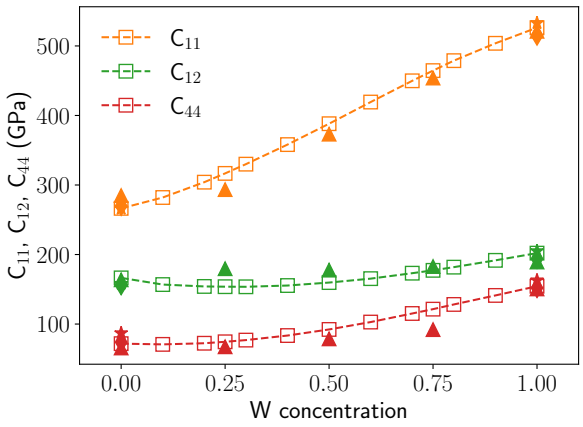

(b) C_{ij}

Figure 7: (a) Variation of the bulk modulus for chemically random W-Ta alloy. Unfilled squares correspond to GEAM results, results from DFT calculations of Ref. [48] are marked using filled triangles and filled circles represent CPA results from Ref. [2]. The experimental and current DFT predictions of the pure systems are marked with filled stars and diamonds respectively. (b) Variation of elastic constants (C_{ij}) for chemically random W-Ta alloy in bcc phase. Unfilled squares correspond to GEAM results and results from DFT calculations [48] are marked using filled triangles. The experimental and current DFT predictions of the pure systems are marked with filled stars and diamonds respectively.

arrangement of 2000 atoms in a $10 \times 10 \times 10$ BCC supercell. The bulk modulus (B) and the elastic constants (C_{ij}) for the bcc phase of W-Ta alloy at different compositions are compared with DFT data for SQS of W-Ta alloy [48] in Fig. 7. While bulk modulus predictions from the current potential are in excellent agreement with DFT data from Ref. [48], results obtained from CPA calculations reported in Ref. [2] are about 10% higher than GEAM and DFT results. Note that structures with hydrostatic and volume conserving tetragonal strains (needed for bulk and shear moduli calculations) are included in the training set only for pure Ta, pure W and two intermediate compositions. Therefore, the excellent agreement with DFT results at compositions not included in the training set further demonstrates the accuracy of the GEAM potential.

The three independent elastic constants, C_{11}, C_{12} and C_{44}, for different compositions shown in Fig. 7 are also predicted within 5% of DFT values reported in Ref. [48]. The elastic constants increase monotonically as the concentration of tungsten increases and as such can be approximated by the following fit.

$$\begin{aligned} C_{11} &= -179.27x_{\mathrm{W}}^3 + 295.30x_{\mathrm{W}}^2 + 145.94x_{\mathrm{W}} + 264.32 \\ C_{12} &= -39.57x_{\mathrm{W}}^3 + 149.09x_{\mathrm{W}}^2 - 69.53x_{\mathrm{W}} + 162.18 \\ C_{44} &= -62.10x_{\mathrm{W}}^3 + 175.95x_{\mathrm{W}}^2 - 31.28x_{\mathrm{W}} + 72.02. \end{aligned} \tag{15}$$

4. Results

After extensive validation of the potential across the entire chemical space, we use the interatomic potential to calculate the effect of chemistry on defect properties, melting points and stability of screw dislocations.

4.1. Stability of ordered structures

To analyze the ground-state (ordered) structures at various compositions, we use our GEAM potential to calculate energies of a few selected low energy crystal structures studied in Ref. [5]. In Fig. 8, we compare the mixing enthalpies obtained by using the GEAM potential, our DFT simulations, DFT values reported in Ref. [5] and those obtained from a Finnis-Sinclair type potential for W-Ta [11]. In contrast to the Finnis-Sinclair type potential developed in Ref. [11], results from our GEAM potential are in much better agreement with DFT results. Note that except for the $B2$ structure for W_6Ta_6, none of the other structures are present in training set. Therefore, this analysis further validates the ability of the potential to extrapolate beyond the training domain.

In addition, consistent with our DFT calculations, the GEAM potential predicts the $C11_b$ structure for W_2Ta is the most stable configuration. This is in variance with DFT results of Ref. [5] where the enthalpy of W_5Ta_3 is about 0.6 meV/atom lower than W_2Ta. This discrepancy between the two DFT results (i.e., this work and those reported in Ref. [5]) can be attributed to the difference in the **k**-point mesh sizes: Our mesh sizes are smaller than the 0.2 Å^{-1} used in Ref. [5] and are obtained by converging the total energies with respect to the number of **k**-points.

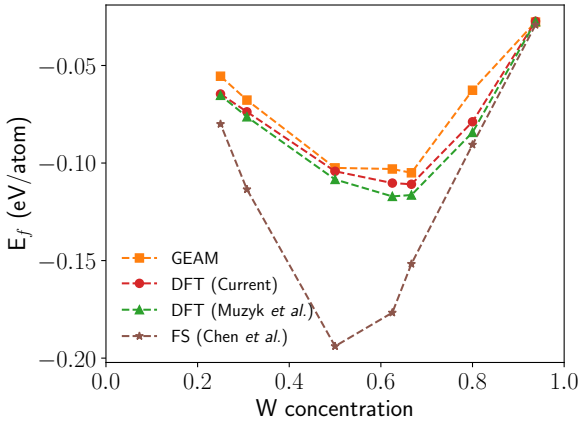

Figure 8: The enthalpy of mixing for low energy crystal structures [5] of W-Ta alloys. Orange squares correspond to GEAM results, enthalpies from current DFT simulations are marked using red circles, green triangles represent DFT results from Ref. [5] and results from the Finnis-Sinclair type interatomic potential model [11] are marked using brown stars.

4.2. Effect of chemistry on vacancy formation energies

We now investigate the formation energies of vacancies for chemically random W-Ta alloys in BCC phase. Note that the vacancy formation energy depends on local chemical environment around the vacant site, which in turn depends on the global chemical composition as well as the distribution of the alloying elements. Therefore, the formation energy of a vacancy, which is formed when a W atom is removed from the structure (in which W and Ta atoms and randomly distributed), is given by the following relation [5]

$$E_f^{\mathrm{vac}}(x_{\mathrm{W}}, \xi_{\mathrm{W}}) = E^{(X-1)\mathrm{W}}(x_{\mathrm{W}}, \xi_{\mathrm{W}}) - E^{X\mathrm{W}}(x_{\mathrm{W}}) + e_{\mathrm{W}}. \tag{16}$$

Here x_{W} is the global composition of W, ξ_{W} is the fraction of W atoms in the nearest neighbourhood (i.e., the first coordination shell) of the vacant site, $E^{(X-1)\mathrm{W}}(x_{\mathrm{W}}, \xi_{\mathrm{W}})$ is the energy of a structure with a vacancy located on a tungsten site for which the local tungsten composition (i.e. W atoms in the first coordination shell surrounding the vacancy) is ξ_{W}, $E^{X\mathrm{W}}(x_{\mathrm{W}})$ is the energy of the defect free W-Ta alloy and e_W is the chemical potential of pure tungsten. The formation energy of a tantalum vacancy is calculated using a similar approach. All formation energy calculations are done using a supercell obtained by replicating the BCC unit cell by 6×6×6 along the three axes and energies are then averaged over 10 different realizations of the chemically random W-Ta alloy to generate the curves shown in Fig. 9. The variations of formation energies of Ta and W vacancies with the local as well as the global tungsten concentrations, i.e. ξ_{W} and x_{W}, respectively, are presented in Fig. 9.

For all the four different global compositions considered in this analysis, the vacancy formation energies (for both tungsten and tantalum) increase with increase in the concentration of tungsten in the first coordination shell. For example, for a tantalum vacancy, the formation energy is lowest in a tantalum rich neighbourhood and increases as the chemical environment

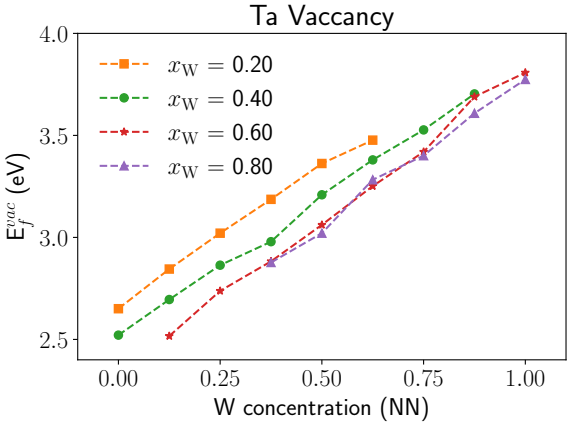

(a)

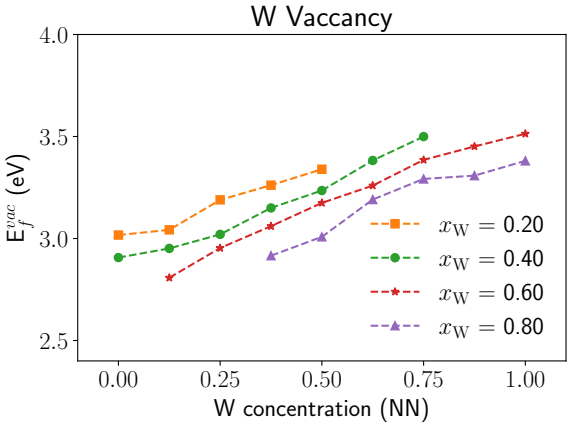

(b)

Figure 9: Formation energies of (a) tantalum and (b) tungsten vacancies as a function of different number of W atoms in the first coordination shell (around the vacant site). The dashed lines correspond to structures with different global concentration of tungsten (denoted by x_W in the legend).

around the vacancy site becomes W rich. This suggests that Ta-W bonds are harder to break meaning that Ta-W mixing is preferred more than Ta-Ta. On the other hand, W-W type bonds are marginally favourable than Ta-W because the W vacancy formation energy also increases with ξ_W. The vacancy formation energies are also influenced by the global chemical composition of the alloy: for the same environment around a defect the formation energy decreases with increasing global composition of tungsten suggesting that interactions with atoms beyond the first coordination shell are also important.

4.3. Melting point of W-Ta alloy

Next, we perform two phase solid-liquid MD simulations to determine the equilibrium melting points of W-Ta alloy at different compositions. To this end, MD simulations are performed using a supercell of $10 \times 10 \times 50$ BCC unit cells with 10000 atoms. The simulation box is first thermalized to a guess melting temperature T_0. One half of the simulation box is then heated to temperature $T_1 > T_0 + 1000$ K so that the solid in

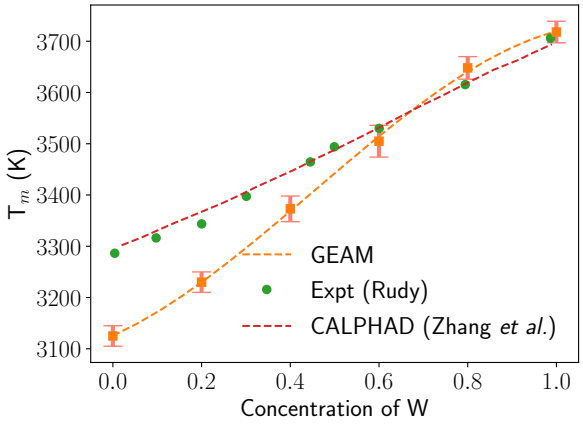

Figure 10: Melting temperatures for chemically random W-Ta alloys. Orange lines with squares are GEAM predictions, experimental data [49] is marked with green circles and red dashed line denote CALPHAD predictions from Ref. [50]. The error bars represent the standard deviation of temperature at the end of the thermalization stage.

this region melts to form a liquid. This liquid region is then cooled back to T_0 while the other solid half is maintained at T_0. Finally, the resulting solid-liquid system is thermalized in the isobaric-isoenthalpic ensemble for about 1 ns. At the end of the thermalization process, if the solid and liquid phases are still present in the simulation box, then the mean temperature during the last 0.2 ns is taken to be the equilibrium melting point. Otherwise, the entire process is repeated with a new guess for T_0. For our analysis, we set T_0 close to the experimental melting point of one of the pure elements [49] and set T_1 to 5000 K to ensure that one half of the system melts.

The melting points predicted from the potential at different compositions of W are shown in Fig. 10. The melting point estimates from experiments [49] and the CALPHAD (CALculation of PHAse Diagram) approach of [50] are also marked in the figure for comparison. While the melting point predictions are generally in reasonable agreement with experimental and CALPHAD results, melting points of tungsten rich alloys are predicted with very high accuracy. The largest disagreement is observed for the melting point of pure tantalum for which the GEAM potential underestimates the melting point by 160 K. This corresponds to a relative error of 5% compared to the experimental data. For reference, the GAP potential for Ta [12] also underestimates the melting point by 8.5% and the predictions of the GAP potential for W-Mo alloy [42] are consistently $5-7\%$ below the experimental values. Therefore, we conclude that the model predictions for melting points are in good agreement with experimental melting points and the accuracy is comparable to existing machine learning potentials.

4.4. Stability of screw dislocations in tantalum and tungsten

Uniaxial compression and tension tests performed on pure single crystals of BCC refractory metals like Ta, Mo, Nb, Fe, etc. suggests that the low temperature deformation mechanisms are governed by the motion of $a_0\langle 111\rangle/2$ screw dislocations,

where a_0 is the lattice parameter, on {112} planes and at little higher temperature on {110} planes [51, 52, 53, 54, 55]. While many possible core structures have been proposed in the literature, detailed atomistic analysis by Suzuki showed that the easy core has lower energy than the hard core geometry. In the subsequent years, this conclusion has been validated by DFT calculations for many BCC refractory metals [56, 57, 58, 59, 60, 61]. However, many interatomic potentials reported in the literature show that the easy core is spatially delocalized which means that the core geometry will have to change to a narrow structure (possibly of higher energy than the delocalized core) in order to move.

To analyze the stability of screw dislocations in Ta and W, we use cylindrical samples with radii 35 Å and height 11 Å and insert screw dislocations with easy and hard configurations at the center of the cylinder with dislocation line directions parallel to the axis of the cylinder, which itself is parallel to $\langle 111 \rangle$. A screw dislocation is inserted by imposing the elastic displacement field such that the Burgers vector is $a_0\langle 111 \rangle/2$ and the lattice parameters are listed in Table 1. The easy and hard-core configurations are simply a manifestation of whether the Burgers vector of the imposed elastic strain field is parallel or anti-parallel to the intrinsic helicity of the BCC lattice along the $\langle 111 \rangle$. In agreement with previous DFT calculations, our results suggest that the easy-core structure is stable for both Ta and W, whereas the hard-core structure is unstable for both metals.

Now, even in a compact easy-core structure there is an additional degree of freedom associated the motion of atoms in the core along the dislocation line direction (say $\hat{\xi}$). Consequently, two types of compact core structures of $a_0\langle 111 \rangle/2$ screw dislocations have been suggested from atomistic simulations: a polarized and an unpolarized core in which the relative displacements $\mathbf{r}_{\langle ij \rangle}$ between the pairs of atoms $\langle ij \rangle$ = (A, A_1), (B, B_1) or, (C, C_1), shown in Fig. 11(a), along $\hat{\xi}$ are all zero, i.e. $\delta_{\langle ij \rangle} = \left(\mathbf{r}_{\langle ij \rangle} \cdot \hat{\xi}\right) = 0$, and (*ii*) a polarized core in which $\delta_{AA_1}, \delta_{BB_1}, \delta_{CC_1}$ are all equal and non-zero, i.e. $\delta_{AA_1} = \delta_{BB_1} = \delta_{CC_1} = \delta \neq 0$. This choice is motivated by the fact that δ is zero in a defect-free supercell and remains unperturbed even after incorporating the displacement field of a screw dislocation.

Since a polarized core involves a lateral translation of the columns of atoms (marked A, B, C in Fig. 11(a)) along the dislocation line, atoms at the locations at which flips in polarity happens can be under tension or compression. This means that at finite temperature polarization flips result in a one dimensional density wave along the dislocation line in the system. While DFT simulations suggest screw dislocation core structures are unpolarized for BCC refractory metals, polarized cores have been reported from analysis done using empirical potentials. Therefore, it is important to assess the energy landscape as a function of displacement of the core atoms. To this end, in Fig. 11(b) we show the change in energy, with respect to the ground-state easy-core structure, as the three columns of atoms marked A, B and C in Fig. 11(a) are displaced along the $\langle 111 \rangle$ direction. For small perturbations about the zero displacement, the energy of the system increases which means that the dislocation cores are unpolarized in both Ta and W.

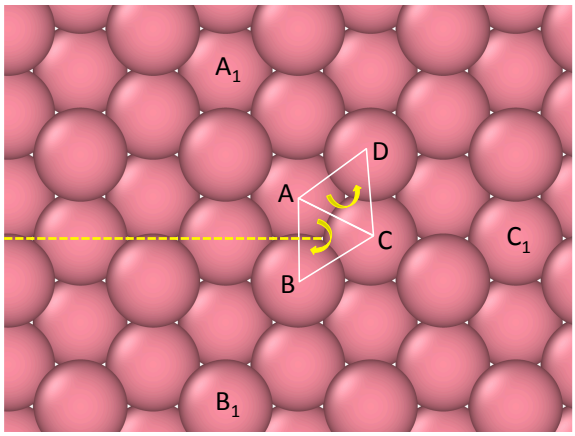

(a)

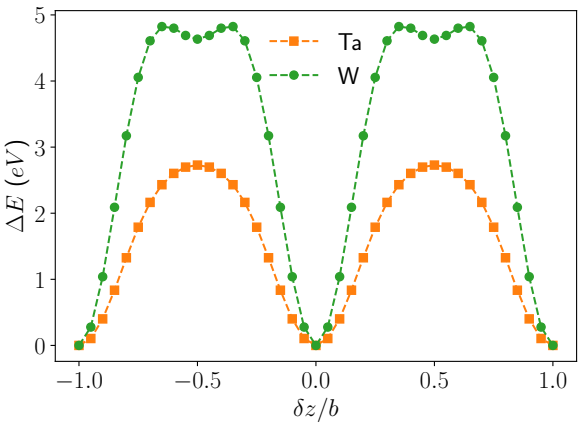

(b)

Figure 11: The atomic arrangement of a defect free supercell viewed along the [111] direction is shown in (a). The yellow arrows inside the two triangles show the opposite helicity in the arrangement of atoms. A screw dislocation can be located at the centers of triangles ABC (by cutting the supercell along the yellow dashed line) or ADC. Depending on the sign of the Burgers vector the center of one triangle (easy core) has lower energy than the other. The relative separation along [111] direction between the atoms pairs (A, A_1), (B, B_1), (C, C_1) is zero in the pristine sample and after the insertion of the dislocation. (b) The change in energy, ΔE, of an easy-core dislocation structure upon the displacement (by δz)of the three columns of atoms A, B and C along the dislocation line.

5. Conclusions

In conclusion, we have developed a potential framework for multi-element system which includes explicit three-body interactions (to capture angular effects), many-body interactions via a generalization of the embedded atom method and a nonlinear many-body interaction term obtained from a symbolic regression analysis. Each term in the GEAM framework, i.e., the embedding energy, three-body and nonlinear many-body interaction terms, are modeled using a set of atom-centered, even-tempered Gaussian basis functions which provides sufficient flexibility to model a diverse set of atomic environments. Majority of the free parameters in the model are learned by solving a system of linear equations which drastically simplifies the model training process in comparison to traditional EAM, MEAM and machine learning potentials based on neural network, graph neural network and the GAP framework. In addition, the total number of structures needed to obtain a reliable model is about one-two orders of magnitude smaller than those needed for most machine learning potentials.

The proposed GEAM framework is then used to develop a potential for the W-Ta alloy. It is shown that the potential predicts physical properties, such as elastic constants, equation of state, melting temperatures and phonon dispersion curves, for pure W and Ta with very high accuracy. The point defect properties, such as formation energies of monovacancies and self-interstitials for pure elements are also predicted with an accuracy on par with single element machine learning potentials, such as SNAP [13, 14] and GAP [12]. The potential is also tested and validated at arbitrary chemical composition of W-Ta alloy to assess the effect of chemistry. While the potential can accurately predict a variety of physical properties for Ta, W and the Ta-W alloys, we summarize below a few notable features: (a) The generalization of the embedding energy term, which is motivated by the model proposed in Ref. [22] helps in improving the accuracy of the model over traditional embedding energy formulations. (b) The explicit three-body interaction term present in our model helps in accurately predicting the phonon dispersion curves even though no structures associated with perturbations along high-symmetry directions are present in the training set. In addition, the coefficients of the angular term are calculated by solving a linear system, which ensures that the optimum coefficients correspond to the global minimum of the loss function. (c) The inclusion of three-body interaction terms to model the effect of chemistry significantly enhances the predictive capability of the model. For example, the formation enthalpies of ordered alloys are very close to those obtained from DFT simulations and the ground-state ordered structure is correctly predicted even though it was not included in the training set. (d) The nonlinear many-body interaction term obtained via symbolic regression helps in predicting the melting temperatures with reasonable accuracy. Here we note that traditional and machine learning potentials often underestimate the melting points by a few hundred Kelvin.

Acknowledgements

This work was performed under the auspices of the U.S. Department of Energy by Lawrence Livermore National Laboratory under Contract DE-AC52-07NA27344. This work was funded by the Laboratory Directed Research and Development (LDRD) Program at LLNL under project tracking code 21-ERD-005. Computing support for this work came from the Lawrence Livermore National Laboratory institutional computing facility. The authors would like to acknowledge Robert Rudd for stimulating discussions and are grateful to Chiraag Nataraj for providing bcc structures (used in training set) obtained from MC simulations at different global W concentrations using cluster-expansion models. LLNL IM release number is LLNL-JRNL-855988.

Appendix A: Training Structures

Structure Type	Pure Ta	Pure W	W-Ta alloy
bcc	1	1	36
Strained bcc	35	42	62
Strained hcp	8	3	
Straineed fcc	6	6	
Vacancies	4	5	22
Interstitials	7	4	12
Surfaces	4	2	
Dislocations	5	2	
Grain boundaries	5		25
Sheared structures	2	6	
Clusters	3	3	
Voids	2	2	
Vacancy loop		1	
High temperature solid	2	2	3
Liquid	2	4	7
Total	86	83	167

Table 4: List of structures included in the training database of the W-Ta potential model. The strained structures include structures with hydrostatic strains ($\leq$ 25%), volume conserving tetragonal strains ($\leq$ 5%) and uniaxial strains ($\leq$ 10%). Structures containing a single vacancy, a di-vacancy (oriented along $\langle 100 \rangle$ or $\langle 110 \rangle$ direction) and a tri-vacancy oriented along $\langle 100 \rangle$ direction are grouped in Vacancy structures. Similarly, structures containing interstitials at octahedral site and $\langle 100 \rangle$, $\langle 110 \rangle$ as well as $\langle 111 \rangle$ dumbbell geometries are grouped in Interstitial structures. To include the effect of curved surfaces, voids (i.e. 51 and 65 atoms removed from a supercell with 432 atoms) and clusters (containing 51, 65 and 169 atoms) are also included in the training set.

Appendix B: Optimized Coefficients

Ω	Ta	W
α_0	0.011337643576920	0.011342489682087
β_0	1.568623266438735	1.568160791507831
$\hat{\alpha}_0$	0.009040116362025	0.009040116362025
$\hat{\beta}_0$	1.827471543693809	1.827471543693809
$\overline{\alpha}_0$	0.013625947956475	0.010723960140263
$\overline{\beta}_0$	1.113947734506080	1.109138895946882

Table 5: List of optimized Gaussian widths Ω for the W-Ta potential model. These parameters correspond to those listed in Eqs. (2), (5) and (9).

	Ta	W
C_0	-4.85575146577716	-1.51900756958284
C_{1n}	2.5624e+05, -1.2314e+06, 2.2639e+06, -2.1295e+06, 1.1515e+06, -3.7917e+05 7.6575e+04, -8.1556e+03	1.0736e+05, 0.0000e+00, -5.4506e+05, 8.3596e+05, -5.7855e+05, 2.2795e+05, -5.4782e+04, 7.2309e+03
C_{2n}	3.5537e+04, 0.0000e+00, -2.1915e+05, 4.0576e+05, -3.7368e+05, 2.2253e+05, -9.4455e+04, 2.6339e+04	-1.1844e+05, 0.0000e+00, 6.9108e+05, -1.2026e+06 1.0063e+06, -5.2710e+05, 1.9307e+05, -4.6515e+04
C_{3n}	1.2442e+06, -3.7304e+06, 4.5528e+06, -3.0363e+06 1.2710e+06, -3.7480e+05, 9.2850e+04, -2.4624e+04	1.7255e+06, -5.3857e+06, 7.0002e+06, -5.1421e+06 2.4737e+06, -8.5534e+05, 2.1172e+05, -1.9387e+04
C_{4n}	-2.4272e+05, 7.4880e+05, -9.5468e+05, 6.8042e+05, -3.1512e+05, 1.0896e+05, -3.6129e+04, 1.7600e+04	-3.1082e+05, 1.0211e+06, -1.4437e+06, 1.2216e+06 -7.4867e+05, 3.9263e+05, -2.0063e+05, 9.5797e+04
$\hat{C}_n$	4.1600e+05, -1.2602e+06, 1.5642e+06, -1.0706e+06 4.6362e+05, -1.3921e+05, 3.0541e+04, -4.4371e+03	-7.4542e+04, 2.5877e+05, -3.8108e+05, 3.1794e+05, -1.6907e+05, 6.0818e+04, -1.5036e+04, 2.2935e+03

Table 6: List of optimized coefficients for the embedding term (E_{em}) of the W-Ta potential model. The coefficients C_{1n} for $n = 1, 2, \ldots, 8$ correspond to C_{1n}^{Ta} and C_{1n}^{W} for $m = 1$ in Eq. (2).

	Ta-Ta-Ta	Ta-Ta-W	Ta-W-W	W-Ta-Ta	W-Ta-W	W-W-W
$\hat{C}_{11}$	-8.1184e+04	-2.5733e+05	-8.2699e+05	178.50	-3.0199e+05	-7.3093e+05
$\hat{C}_{12}$	2.3523e+05	7.4226e+05	2.4103e+06	0.0000000	8.8273e+05	2.1405e+06
$\hat{C}_{13}$	-5.8939e+04	-1.6161e+05	-5.2566e+05	1.2260e+04	-1.8221e+05	-4.6245e+05
$\hat{C}_{14}$	-1.1364e+04	-6.6340e+04	-2.4398e+05	-1.1165e+04	-1.0075e+05	-2.3008e+05
$\hat{C}_{22}$	-1.4453e+05	-4.6696e+05	-1.5371e+06	-8072.0	-5.7156e+05	-1.3766e+06
$\hat{C}_{23}$	0.0000000	0.0000000	0.0000000	0.0000000	0.0000000	0.0000000
$\hat{C}_{24}$	4.8991e+04	1.9247e+05	6.9113e+05	1.3297e+04	2.6912e+05	6.4122e+05
$\hat{C}_{33}$	5.9937e+04	1.7355e+05	5.8599e+05	-3581.5	2.1356e+05	5.2851e+05
$\hat{C}_{34}$	-5.8199e+04	-1.8619e+05	-6.6421e+05	-3434.4	-2.5086e+05	-6.1347e+05
$\tilde{C}_{44}$	1.0066e+04	3.0146e+04	1.1055e+05	522.43	4.1965e+04	1.0333e+05

Table 7: List of optimized coefficients ($\hat{C}_{mn}^{e_i e_j e_k}$) for the radial component of the three-body term ($\hat{E}_{32}$) of the W-Ta potential model. The coefficients $\hat{C}$ correspond to those listed in Eq. (5)

.

c_1	c_2	c_3	c_4	c_5	c_6	c_7	c_8	c_9	c_{10}	c_{11}	c_{12}
-12.32	-73.32	64.22	923.42	45.99	-3214.42	-1056.66	4121.66	1771.44	-2011.66	-775.96	282.93

Table 8: List of optimized angle coefficients (c_p) for the three-body term of the W-Ta potential model. The coefficients c_p for $p = 1, 2...., 12$ correspond to those listed in Eq. (6).

$\overline{C}_n^1$	-8.2309e+05, 1.3873e+06, 0.0000e+00, -7.3814e+05, 0.0000e+00, 1.7392e+05
$\overline{C}_n^2$	-5.9258e+05, 1.3017e+06, 0.0000e+00, -1.9897e+06, 1.7306e+06, -4.5003e+05
$\overline{C}_n^3$	4.5318e+05, -7.6641e+05, 0.0000e+00, 4.1077e+05, 0.0000e+00, -9.7528e+04

Table 9: List of optimized coefficients ($\overline{C}_n$) for the non-local term (E_{nl}) of the W-Ta potential model. The coefficients $\overline{C}_n$ for $n = 1, 2, ..., 6$ correspond to those listed in Eq. (7)

Data availability

The processed data and code for the Ta-W potential required to reproduce the findings are available in the supplementary materials.

References

[1] I. S. Winter, M. de Jong, J. Montoya, E. Rothchild, D. C. Chrzan, Intrinsic ductility of random substitutional alloys from nonlinear elasticity theory, Phys. Rev. Materials 3 (2019) 113608. doi:10.1103/PhysRevMaterials.3.113608.

[2] P. Turchi, A. Gonis, V. Drchal, J. Kudrnovskỳ, First-principles study of stability and local order in substitutional ta-w alloys, Physical Review B 64 (8) (2001) 085112.

[3] G. L. Hart, V. Blum, M. J. Walorski, A. Zunger, Evolutionary approach for determining first-principles hamiltonians, Nature materials 4 (5) (2005) 391–394.

[4] V. Blum, A. Zunger, Prediction of ordered structures in the bcc binary systems of mo, nb, ta, and w from first-principles search of approximately 3,000,000 possible configurations, Physical Review B 72 (2) (2005) 020104.

[5] M. Muzyk, D. Nguyen-Manh, K. Kurzydłowski, N. Baluc, S. Dudarev, Phase stability, point defects, and elastic properties of wv and w-ta alloys, Physical Review B 84 (10) (2011) 104115.

[6] J. Rumble, Crc handbook of chemistry and physics (100th ed.). boca rotan, fl (2019).

[7] Y. Li, D. J. Siegel, J. B. Adams, X.-Y. Liu, Embedded-atom-method tantalum potential developed by the force-matching method, Physical Review B 67 (12) (2003) 125101.

[8] M.-C. Marinica, L. Ventelon, M. Gilbert, L. Proville, S. Dudarev, J. Marian, G. Bencteux, F. Willaime, Interatomic potentials for modelling radiation defects and dislocations in tungsten, Journal of Physics: Condensed Matter 25 (39) (2013) 395502.

[9] B.-J. Lee, M. Baskes, H. Kim, Y. K. Cho, Second nearest-neighbor modified embedded atom method potentials for bcc transition metals, Physical Review B 64 (18) (2001) 184102.

[10] Y. Chen, Y.-H. Li, N. Gao, H.-B. Zhou, W. Hu, G.-H. Lu, F. Gao, H. Deng, New interatomic potentials of w, re and w-re alloy for radiation defects, Journal of Nuclear Materials 502 (2018) 141–153.

[11] Y. Chen, J. Fang, L. Liu, W. Hu, N. Gao, F. Gao, H. Deng, Development of the interatomic potentials for w-ta system, Computational Materials Science 163 (2019) 91–99.

[12] J. Byggmästar, K. Nordlund, F. Djurabekova, Gaussian approximation potentials for body-centered-cubic transition metals, Physical Review Materials 4 (9) (2020) 093802.

[13] A. P. Thompson, L. P. Swiler, C. R. Trott, S. M. Foiles, G. J. Tucker, Spectral neighbor analysis method for automated generation of quantum-accurate interatomic potentials, Journal of Computational Physics 285 (2015) 316–330.

[14] M. A. Wood, A. P. Thompson, Quantum-accurate molecular dynamics potential for tungsten, arXiv preprint arXiv:1702.07042.

[15] Y.-S. Lin, G. P. P. Pun, Y. Mishin, Development of a physically-informed neural network interatomic potential for tantalum, Computational Materials Science 205 (2022) 111180.

[16] G. P. Pun, K. Darling, L. Kecskes, Y. Mishin, Angular-dependent interatomic potential for the cu–ta system and its application to structural stability of nano-crystalline alloys, Acta Materialia 100 (2015) 377–391.

[17] M. S. Daw, M. I. Baskes, Semiempirical, quantum mechanical calculation of hydrogen embrittlement in metals, Physical review letters 50 (17) (1983) 1285.

[18] M. S. Daw, M. I. Baskes, Embedded-atom method: Derivation and application to impurities, surfaces, and other defects in metals, Physical Review B 29 (12) (1984) 6443.

[19] Y. Mishin, A. Lozovoi, Angular-dependent interatomic potential for tantalum, Acta Materialia 54 (19) (2006) 5013–5026. doi:https://doi.org/10.1016/j.actamat.2006.06.034.

[20] A. P. Bartók, M. C. Payne, R. Kondor, G. Csányi, Gaussian approximation potentials: The accuracy of quantum mechanics, without the electrons, Phys. Rev. Lett. 104 (2010) 136403. doi:10.1103/PhysRevLett.104.136403.

[21] J. Behler, M. Parrinello, Generalized neural-network representation of high-dimensional potential-energy surfaces, Phys. Rev. Lett. 98 (2007) 146401. doi:10.1103/PhysRevLett.98.146401.

[22] A. Takahashi, A. Seko, I. Tanaka, Conceptual and practical bases for the high accuracy of machine learning interatomic potentials: application to elemental titanium, Physical Review Materials 1 (6) (2017) 063801.

[23] Y. Mishin, Machine-learning interatomic potentials for materials science, Acta Materialia 214 (2021) 116980. doi:https://doi.org/10.1016/j.actamat.2021.116980.

[24] Y. Zuo, C. Chen, X. Li, Z. Deng, Y. Chen, J. Behler, G. CsÃ¡nyi, A. V. Shapeev, A. P. Thompson, M. A. Wood, S. P. Ong, Performance and cost assessment of machine learning interatomic potentials, The Journal of Physical Chemistry A 124 (4) (2020) 731–745.

[25] P. M. Derlet, D. Nguyen-Manh, S. Dudarev, Multiscale modeling of crowdion and vacancy defects in body-centered-cubic transition metals, Physical Review B 76 (5) (2007) 054107.

[26] P.-W. Ma, S. Dudarev, Symmetry-broken self-interstitial defects in chromium, molybdenum, and tungsten, Physical Review Materials 3 (4) (2019) 043606.

[27] H. Ullmaier, Atomic defects in metals, condensed matter (1991).

[28] Y. S. Teh, L. H. Yang, B. Sadigh, S. Hamel, V. Bulatov, A. Samanta, Analysis of high-pressure phase stability in iron using a generalized embedded atom method interatomic potential, Submitted to Physical Review B.

[29] I. Cherkes, S. Klaiman, N. Moiseyev, Spanning the hilbert space with an even tempered gaussian basis set, International Journal of Quantum Chemistry 109 (13) (2009) 2996–3002.

[30] A. Seko, A. Takahashi, I. Tanaka, Sparse representation for a potential energy surface, Physical Review B 90 (2) (2014) 024101.

[31] C. Reeves, M. Harrison, Use of gaussian functions in the calculation of wavefunctions for small molecules. ii. the ammonia molecule, The Journal of Chemical Physics 39 (1) (1963) 11–17.

[32] R. D. Bardo, K. Ruedenberg, Even-tempered atomic orbitals. vi. optimal orbital exponents and optimal contractions of gaussian primitives for hydrogen, carbon, and oxygen in molecules, The Journal of Chemical Physics 60 (3) (1974) 918–931.

[33] E. R. Davidson, D. Feller, Basis set selection for molecular calculations, Chemical Reviews 86 (4) (1986) 681–696.

[34] G. Wu, G. Lu, C. J. García-Cervera, E. Weinan, Density-gradient-corrected embedded atom method, Physical Review B 79 (3) (2009) 035124.

[35] T. J. Lenosky, B. Sadigh, E. Alonso, V. V. Bulatov, T. D. de la Rubia, J. Kim, A. F. Voter, J. D. Kress, Highly optimized empirical potential model of silicon, Modelling and Simulation in Materials Science and Engineering 8 (6) (2000) 825.

[36] H. Zong, G. Pilania, X. Ding, G. J. Ackland, T. Lookman, Developing an interatomic potential for martensitic phase transformations in zirconium by machine learning, npj Computational Materials 4 (1) (2018) 1–8.

[37] S.-M. Udrescu, M. Tegmark, Ai feynman: A physics-inspired method for symbolic regression, Science Advances 6 (16) (2020) eaay2631.

[38] M. Cranmer, A. Sanchez Gonzalez, P. Battaglia, R. Xu, K. Cranmer, D. Spergel, S. Ho, Discovering symbolic models from deep learning with inductive biases, in: H. Larochelle, M. Ranzato, R. Hadsell, M. Balcan, H. Lin (Eds.), Advances in Neural Information Processing Systems, Vol. 33, Curran Associates, Inc., 2020, pp. 17429–17442.

[39] D. P. Searson, GPTIPS 2: An Open-Source Software Platform for Symbolic Data Mining, Springer International Publishing, Cham, 2015, pp. 551–573. doi:10.1007/978-3-319-20883-1$_2$2.

[40] G. Kresse, J. Hafner, Ab initio molecular dynamics for liquid metals, Physical review B 47 (1) (1993) 558.

[41] G. Kresse, D. Joubert, From ultrasoft pseudopotentials to the projector augmented-wave method, Physical review b 59 (3) (1999) 1758.

[42] G. Nikoulis, J. Byggmästar, J. Kioseoglou, K. Nordlund, F. Djurabekova, Machine-learning interatomic potential for w–mo alloys, Journal of Physics: Condensed Matter 33 (31) (2021) 315403.

[43] A. P. Thompson, H. M. Aktulga, R. Berger, D. S. Bolintineanu, W. M. Brown, P. S. Crozier, P. J. in't Veld, A. Kohlmeyer, S. G. Moore, T. D. Nguyen, et al., Lammps-a flexible simulation tool for particle-based materials modeling at the atomic, meso, and continuum scales, Computer Physics Communications 271 (2022) 108171.

[44] P. Söderlind, O. Eriksson, J. Wills, A. Boring, Theory of elastic constants of cubic transition metals and alloys, Physical Review B 48 (9) (1993) 5844.
[45] A. Togo, I. Tanaka, First principles phonon calculations in materials science, Scr. Mater. 108 (2015) 1–5.
[46] M. Čák, T. Hammerschmidt, J. Rogal, V. Vitek, R. Drautz, Analytic bond-order potentials for the bcc refractory metals nb, ta, mo and w, Journal of Physics: Condensed Matter 26 (19) (2014) 195501.
[47] R. Krishnan, S. Garg, N. Krishnamurthy, The tantalum–tungsten system, J. Alloy Phase Diagrams 3 (1) (1987) 1–3.
[48] N. Wei, T. Jia, X. Zhang, T. Liu, Z. Zeng, X. Yang, First-principles study of the phase stability and the mechanical properties of w-ta and w-re alloys, AIP Advances 4 (5) (2014) 057103.
[49] E. Rudy, Compendium of phase diagram data, air force materials laboratory, wright-patterson afb, oh, rep. no, Tech. rep., AFML-TR-65-2, Part (1969).
[50] E. Zhang, Y. Tang, M. Wen, A. Obaied, I. Roslyakova, L. Zhang, On phase stability of mo-nb-ta-w refractory high entropy alloys, International Journal of Refractory Metals and Hard Materials 103 (2022) 105780.
[51] M. S. Duesbery, R. A. Foxall, A detailed study of the deformation of high purity niobium single crystals, Philosophical Magazine 20 (166) (1969) 719–751.
[52] A. Seeger, C. Wüthrich, Dislocation relaxation processes in body-centred cubic metals, Il Nuovo Cimento B (1971-1996) 33 (1) (1976) 38–75.
[53] H. Mizubayashi, M. Morita, T. Kakihara, S. Okuda, Anelastic study of screw-dislocation motion in high-purity niobium, Acta Metallurgica et Materialia 40 (10) (1992) 2651 – 2659.
[54] A. Luft, L. Kaun, Electron microscopic investigation of the dislocation structure in molybdenum single crystals deformed in tension at 293 and 493 degrees, Physica Status Solidi (b) 37 (2) (1970) 781–793.
[55] A. Seeger, U. Holzwarth, Slip planes and kink properties of screw dislocations in high-purity niobium, Philosophical Magazine 86 (25-26) (2006) 3861–3892.
[56] V. Vitek, Core structure of screw dislocations in body-centred cubic metals: relation to symmetry and interatomic bonding, Philosophical Magazine 84 (2004) 415.
[57] C. Woodward, S. I. Rao, Flexible ab initio boundary conditions: Simulating isolated dislocations in bcc mo and ta, Phys. Rev. Lett. 88 (2002) 216402.
[58] F. Shimizu, S. Ogata, H. Kimizuka, T. Kano, J. Li, H. Kaburaki, First-principles calculation on screw dislocation core properties in bcc molybdenum, Journal of the Earth Simulator 7 (2007) 17–21.
[59] S. Chiesa, M. R. Gilbert, S. L. Dudarev, P. M. Derlet, H. V. Swygenhoven, The non-degenerate core structure of a ½⟨111⟩ screw dislocation in bcc transition metals modelled using finnis–sinclair potentials: The necessary and sufficient conditions, Philosophical Magazine 89 (34-36) (2009) 3235–3243.
[60] E. Clouet, L. Ventelon, F. Willaime, Dislocation core energies and core fields from first principles, Phys. Rev. Lett. 102 (2009) 055502.
[61] L. Dezerald, L. Ventelon, E. Clouet, C. Denoual, D. Rodney, F. Willaime, Ab initio modeling of the two-dimensional energy landscape of screw dislocations in bcc transition metals, Phys. Rev. B 89 (2014) 024104.